Determining constraints imposed by salt fabrics on the morphology of solution mined cavities in relation to CAES, through dissolution experiments using brine and seawater in halite

L.P. Field[1]*, A.E. Milodowski[1], D. Evans[1], B. Palumbo-Roe[1], M.R. Hall[1,2], A.L. Marriott[1], T. Barlow[1], A. Devez[1],

[1] British Geological Survey, Environmental Science Centre, Keyworth, NG12 5GG, UK

[2] The University of Nottingham, Nottingham Centre for Geomechanics, Faculty of Engineering, University Park, Nottingham, NG7 2RD, UK

LPF ORCID iD: 0000-0002-8747-9901

MH ORCHID iD: 0000-0003-1777-3774

*Correspondence lorfie@bgs.ac.uk,

Abbreviated title: Constrains of salt fabrics in dissolution experiments

Abstract:

Large-scale compressed air energy storage facilities offer one solution to the UK's energy demands, using solution-mined caverns in salt lithologies. For optimum gas storage efficiency, cavern geometry should ideally be smooth: spherical to cylindrical with a circular cross-section. However, such caverns are often irregular with marked asymmetry or ellipticity, and whilst the reasons for non-circular cross-sections developing during solution-mining in some caverns can be related to e.g. the presence of interbedded lithologies, in other instances they are not fully understood.

Cavities from dissolution experiments using five main end-member salt facies fabrics from the Triassic Preesall and Northwich Halite formations have been assessed to determine factors affecting cavity geometry, formation and variability in dissolution behaviour. Identical sets of experiments were performed on each fabric type, using two solution concentration strengths: brine and synthetic seawater.

Comparison of experimental results using a combination of analytical and imaging techniques show the extent to which the salt fabric and enhancement of features within the salt influences the resulting dissolution cavity. Observations show a visible increase in micropores within the adjacent halite matrix following dissolution. Smaller-scale features provide further insights into the dissolution processes, and salt fabric behaviour under different dissolution conditions.

Supplementary material: A detailed methodology is available at https://doi.org/xxxx

Introduction:

The growing contribution to UK electricity generation from renewable energy technologies, such as solar photovoltaics (PV) and wind power, will require a parallel development of grid-scale energy storage facilities to balance grid demand. In addition, there is an increasing need to be able to store natural gas (and in future hydrogen) underground in order to meet the UK's energy demands and ensure its energy security. One solution lies in creating large-scale, underground, compressed-air energy storage (CAES) facilities.

Storage of hydrocarbons (including natural gas and liquified petroleum gas) is well established within a number of geologically differing environments such as non-potable (saline) aquifers, depleted oil and gas fields, and to a lesser extent, abandoned mines, lined hard rock caverns and refrigerated mined caverns (Lord, 2009). Particularly in the case of hydrogen storage, solution-mined salt cavities are considered an optimal choice due to the minimal contamination of the hydrogen by the salt (Crotogino and Huebner, 2008; Lord, 2009). CAES, a bulk storage process by which excess electrical energy, generated during periods of off-peak demand, is used to compress air, and store this for release as required during periods of peak-demand, also utilises solution-mined salt caverns at two sites: at Huntorf in northern Germany and McIntosh in Alabama, USA (e.g. Evans, 2007; Crotogino et al., 2001; Crotogino and Huebner, 2008; Goodman, 1992; Leith, 2001). General Compression, together with ConocoPhillips, developed a third such demonstration project using a salt cavern at Gaines in Texas (Currey, 2012). The project was commissioned in late 2012, but is understood to have ceased operation in 2016. Despite a number of lithologies, including massively-bedded halite ('salt beds') offering storage potential, no CAES plants currently exist in the UK.

Halite, or "rock-salt" is highly soluble and readily lends itself to solution mining to create storage caverns. Halite has a number of characteristics making it an ideal material for storage of gas, which is recognised by the British and European standard for gas storage BS EN1918-3:1998 (BS 1998). Key properties include very low permeability and its visco-plastic, self-healing behaviour, which provides a gas-tight environment hundreds of meters below ground (e.g. BS 1998; Warren, 2006). In the UK, the development and distribution of onshore halite beds, together with the locations of currently operational and planned gas storage cavern facilities are outlined in Evans and Holloway (2009) and Evans (2016). Solution-mined salt caverns are already being utilised for natural gas storage, and are being considered for the development of CAES, within the Permian and Triassic bedded halite deposits, both onshore (e.g. Cheshire Basin, Lancashire, Dorset, East Yorkshire and Northern Ireland), and offshore (East Irish Sea Basin). A salt cavern-hosted CAES plant, at Larne in Northern Ireland is currently at an advanced planning stage, being in part EU-funded (Gaelectric, 2015).

Ideal storage cavern geometries are spherical to cylindrical in shape, with smooth cavern walls that permit least disturbed gas flows and provide the greatest volume for the minimal cross-sectional area 'footprint'. However cylindrical caverns are rarely if ever produced, with some developing less than ideal elliptical geometries (e.g. Hauterives, SE France: George et al., 1974), and / or highly irregular shapes extending up-dip (e.g. at Veendam, Netherlands: Fokker et al., 2000 Geluk et al., 2007). Anecdotal evidence from salt caverns in the Cheshire Basin suggests that cavern geometry may be dictated by whether they were developed for brine extraction or gas storage purposes. Caverns produced as a result of brine extraction over decadal timescales tend to develop more elliptical or irregular shapes (A Stacey (Stag Energy) pers. comm.). In contrast, gas storage caverns developed over a shorter period of time (typically 2-3 years), employing less concentrated brines or saline water, and modern cavern construction programmes develop smoother walls and a more "circular" cross-section (Charnavel, 2012; Charnavel et al., 2015).

In addition, dissolution behaviour and the resulting morphology of solution-mined caverns in halites may be influenced by various factors related to the characteristics and properties of the rock itself, including: the presence, thickness and orientation of bedded insoluble lithologies (e.g. mudstones, dolomite and anhydrite); the fabric of the salt and distribution of coarse-grained halite, friable salts or more insoluble materials (e.g. clay, sand, anhydrite grains: Kupfer, 1990; Looff et al., 2010 a & b); more soluble potassium and magnesium salts which may enhance dissolution; grain fabric (size, shape and preferred orientation of the grains, whereby these are a reflection of stress (Bates and Jackson, 1987)); salt microstructure related to deformation, pressure solution and recrystallization mechanisms (e.g.

Carter et al., 1993; Hickman and Evans, 1995a,b); the orientation and irregularity of the dissolving halite surface (e.g. Durie and Jessen, 1964), and; the presence and behaviour of fluid inclusions (e.g. Bein et al., 1991; Roedder, 1984; Raeside, 2003).

The aim of this work was to perform laboratory-scale, flow-through dissolution experiments using pre-drilled salt cores from the Preesall Halite in NW England, to investigate the influence of both end-member salt fabrics and solution salinity, on the dissolution rates and form, of the final cavern morphology.

Materials and Methods:

Sampling of salt core

Two borehole cores held within the National Geological Materials Collection (NGMC) collection at BGS, Keyworth were sampled (Table 1). These cores were both recovered from boreholes drilled through Triassic halite in the NW of England (formed ~245 Mya): The Arm Hill No. 1 borehole (Lat. 53.9119788196, Long. -2.99077338532) in the Preesall Saltfield at the margin of the East Irish Sea Basin in Lancashire and which has a drilled length of 609 m, with 341 m through the Preesall Halite; and the Northwich Victoria Infirmary borehole (Lat. 53.2568729118, Long. -2.52039762053) in the Cheshire Basin, which has a drilled length of 129.5 m through the Northwich Halite. The Preesall Halite and Northwich Halite are lateral equivalents (Wilson and Evans, 1990; Wilson, 1993; Warrington et al., 1999) and these lithologies were selected as both have been used, or are being considered, for gas storage (Evans and Holloway, 2009; Evans, 2016). From the core, two adjacent lengths of core (each 100 mm long) were selected to capture each lithological variation. This was to ensure that the two samples were as alike in fabric as is feasible. The diameter of the Arm Hill and the Northwich cores varied (85 and 105 mm respectively), but otherwise the dimensions of the experimental core blocks were identical. Five key salt end-member facies fabrics (refer Hough et al., 2011) were identified (Figure 1), ranging from almost pure halite (cumulate and primary founded mat, to a high mud content (>80%: Haselgebirge), with intermediate chicken-wire fabric containing anhydrite and clays. The final fabric is a sheared salt, (from a faulted interval) which we refer to here as 'mylonite'.

Experimental set-up

The experimental setup is shown in Figure 2. The 4 mm diameter pilot-hole was drilled longitudinally along the centre of the core, in part analogous to the pilot borehole present within a full-scale cavern. Salt solution was injected into the pilot-hole from the top by a peristaltic pump at a constant flow rate of 0.58 ± 0.02 ml/min and a temperature of 23 ±1 ^{o}C. Two solutions were used for the experiments: experimental set A used a brine with a concentration of 270 g/l NaCl; and experimental set B used a commercially available artificial seawater (D-D H_2O Ocean Pro+ Aquarium Salt: 24 g/l NaCl). Sodium fluorescein was also used in the inlet fluid as a fluorescent tracer dye to monitor the extent of any fluid penetration into the matrix of the salt wallrock adjacent to the resulting solution cavity. One core sample of each of the five end-member fabrics was used with each fluid type.

The duration of the experiments varied across the experimental runs: experiments were terminated when the total volume of the dissolution cavity had reached at least 10 times that of the original pilot hole (~ 1250 mm^3) at the start of the experiment. Experimental set B were of shorter duration because of the anticipated faster salt dissolution rates with the more dilute seawater solution. For experimental runs longer than 7 hours the pumping of fluid was paused overnight, and the salt core

drained and weighed, with the fluid injection being resumed the following day. This allowed tighter control of the dissolution experiment conditions, particularly to prevent fluid loss by seepage through the bottom or top caps, and uncontrolled breaching the wall of the salt core itself. The whole salt core assembly was weighed both at the start and at the end of each leaching period to estimate the rate of mass loss during the dissolution experiments.

After passing through the salt cores, the fluids at the bottom outlet were continuously collected for analysis in 15ml to 30 ml tubes, using an automated fraction collector. A detailed explanation of the experimental set-up is provided in Supplementary Document A.

Analytical Methods

Full details of the analytical methods are provided in Supplementary Document A.

Chloride concentration, fluid density, volumetric flow rate, and temperature of the effluent solutions were measured. Electrical conductivity using a Toledo SevenGo pro™ SG7 conductivity meter with probe InLab® 738 (conductivity range 0.001 to 100 mS/mm), was measured for all the seawater experiments, and also for the for the brine primary founded mat and mylonite experimental samples only, the brine experiments were expected to show very similar results. In addition, the effluent solutions were analysed for major and trace cations by inductively-coupled plasma mass-spectrometry (ICP-MS) and for anions by ion chromatography (IC). The progress of the halite dissolution during the operation of the experiments was monitored by measuring the chloride concentration for a sub-set of effluent brine samples, using a hand-held "chloride ion selective" probe (calibrated against chloride concentrations determined by IC).

A series of imaging techniques were used to selectively assess samples both pre and post-experiment. 2D X-ray radiography using a GE Inspection ISOVOLT Titan E X-ray generator, allowed initial rapid assessment of the experimental cavities. High resolution scans of the samples both pre and post-experiment were obtained with 3D X-ray computed tomography (X-ray CT) using an XRADIA Versa XRM500 (Carl Zeiss, Oberkochen, Germany) instrument, which were processed post-image using Avizo Fire software (v8.1 FEI Inc., Hillsboro, Oregon, USA). Post-experiment cores were dry-sawn in half lengthways and the cut surfaces then imaged by laser-stimulated scanning fluorescence imaging (LSSFI) with an Amersham Biosciences STORM™ 860 laser scanning system (using 635 nm (red) and 450 nm (blue) wavelength excitation and 650 nm and 520 nm low-pass wavelength filters, respectively), to determine the location of any fluorescein tracer, and therefore the extent of fluid penetration into the wallrock matrix. The morphology of the cavities exposed in the half cores were also imaged in 3D using a NextEngine 2020i laser scanner with Scan Studio HD Pro software to produce 3D model of the cavity surface.

Detailed optical and scanning electron microscopy was carried out on both the original halite core samples, the reacted (dissolved and etched) halite surfaces and petrographic polished thin sections prepared from the reacted cores. Etched halite surfaces within the cavities were examined by an Olympus SZX10 optical binocular microscope fitted with an Olympus XC30 digital camera. Higher resolution observations were made by secondary electron (SE) imaging using an FEI QUANTA 600 environmental scanning electron microscope (SEM) equipped with an Oxford Instruments INCA 450 energy-dispersive X-ray microanalysis (EDXA) system to aid mineral identification during SEM observation. Optical petrographic analysis of polished thin sections was undertaken using a Zeiss Axioplan 2 polarising microscope with Zeiss Axiocam MRc5 digital camera, and by backscattered electron (BSE) imaging using the FEI QUANTA 600 environmental scanning electron microscope.

Observations and Results:

Petrology of the salt starting materials

The five end-member fabrics were characterised and key features identified:

Primary founded mat facies

The primary founded mat sample is a near-pure halite rock comprising bands of identifiable elongated crystals in hand specimen (<20 mm), interspersed with minor, fine, red-brown and grey muddy seams and laminations (Figure 1A). Thin section analysis show these fine laminae comprise of clay and anhydrite inclusions (<50 µm). Euhedral fluid inclusions (<40 µm) are also common, reflecting the cubic crystallography of the halite. This primary sedimentary texture is derived from a combination of halite rafts that formed from the aggregation of suspended crystals originally growing on the water surface, which then sank when too large and heavy to be supported by surface tension. Subsequently, when the water was sufficiently shallow, subaqueous halite nucleation and upward growth continued on the upper surfaces of the foundered mats (Arthurton, 1973). The outer part of the core sample showed minor surface dissolution along grain boundaries induced by the drilling fluid, giving a slightly pitted appearance.

Cumulate halite facies

The halite cumulate (Figure 1B) is a near-pure halite and is identified by an even, horizontal banding defined in hand sample by variation in colour (red-brown to colourless). The layered texture reflects the primary sedimentary deposition and steady accumulation of halite crystals. The slight colour variations in hand sample are probably due to slight impurities contained within each layer e.g. minor disseminated detrital clay, hematite, and anhydrite. In thin section, halite crystals are euhedral to subhedral (<15 mm). Inclusions of clays and anhydrite are present around the crystals at grain boundaries and within the halite crystals themselves. Rare crystals of dolomite (<70 µm) and euhedral quartz (<80 µm) are also present. Porosity is present along grain boundaries and halite cleavage planes, and also as isolated pore spaces between halite crystals. Fluid inclusions are abundant and are generally euhedral reflecting the cubic halite crystal structure. No signs were observed of dissolution on the surface of the core as a result of the drilling.

Mylonite halite

This sample is halite dominated, but has been subjected to shear due to faulting, and as a result displays marked, banding along its length at an acute angle to the core axis (Figure 1C). In thin section the rock displays coarse, elongated halite crystals (<20 mm) defining an extension lineation, with some minor clay laminae or films. These laminae define a pre-existing texture that does not correspond to the present halite crystal boundaries, implying that this halite fabric has recrystallised after shearing. Crystals are generally inclusion-rich with both spherical and elongate, elliptical fluid inclusions. A few, rare crystals are inclusion-free which may result from recrystallisation. Some porosity is observed along halite grain boundaries and cleavage planes.

Chicken-wire halite facies

This “chicken-wire” halite sample comprises coarse, subhedral halite crystals (<50 mm) enclosed within a network of thin clay “stringers” or “seams” (Tucker, 2001), which also contain some fine-grained anhydrite crystals (<500 µm: Figure 1D). The halite crystals formed below the brine-substrate interface and displaced the muddy layers around the halite crystals. The surface of the core shows a slight topographical difference between the halite and the muddy layers, with the muddy layers standing slightly proud of the halite, where the soluble halite has been eroded by the drilling fluid during core recovery. In thin section, the relationship between the halite crystals and the clay layers is clearly visible.

Haselgebirge facies

A Haselgebirge texture is defined by 45-85% halite (Spötl 1989), interspersed within thick muddy horizons (in these samples up to 40 mm thick). The core surface has suffered marked dissolution of halite induced during the drilling process, leaving the muddy horizons standing up to 4 mm proud of the dissolved halite surface (Figure 1E). In some instances, the dissolution has sharply undercut the base of the muddy horizon, but has a gentle halite slope above. Optical and SEM analysis confirm these observations. The halite is also pockmarked with depressions produced around small inclusions of insoluble material. The irregular muddy seams and laminations forming the clay "meshwork" have clearly been pushed aside during displacive halite crystal growth, and this is observed in both hand specimen and thin section. The euhedral halite crystals are finer-grained than in the other end-member fabrics (<10 mm), and contain numerous fluid inclusions. Bands of discrete dolomite crystals (<70 µm) are present along some halite grain boundaries. The muddy horizons are compact and dense, and comprise detrital clay and acicular crystals of anhydrite (<50 µm).

General morphology of the experimental cavities

Experimental set A (brine)

X-ray radiography revealed that each resulting dissolution cavity was morphologically unique, and no cavity was formed by uniform dissolution along its length (Figure 3, A1-5). The cumulate halite core produced the most uniform shaped dissolution cavity, and most closely approached a cylinder in shape (Figure 3, A1), which is the "idealised" shape of a full-size storage cavern. This type of halite is the most homogeneous and uniform in mineralogy and texture, comprising almost pure halite. However, the halite dissolution was limited in the uppermost part of the core, with significant dissolution and lateral widening of original pilot hole only occurring below about 20 mm from the fluid inlet point (Figure 3, A1). In addition, the walls of the cavity are stepped horizontally, and also taper downwards slightly towards the fluid outlet point. This halite is relatively homogeneous but does display some colour banding reflecting the distribution of minor impurities (Figure 1B). However, no obvious correspondence was observed between the colour banding and the stepped dissolution morphology.

Dissolution of the primary founded mat core produced a very marked, obliquely-inclined, inverted cone-shaped cavity. Its roof is defined by a thin seam of dolomitic mudstone and organic material in the upper part of the core (clearly illustrated by LSSFI, Figure 4C), and dissolution below this progressively tapers downwards to a narrow base approximately 4 times wider than the pilot hole. The dissolution in the Haselgebirge facies halite sample produced two discrete cavities within halite, separated by a thick layer of dolomitic mudstone interbedded with the halite, and occupying the centre of the core (Figure 3, A4). This mudstone comprises largely insoluble material with very little halite. Consequently, halite dissolution only occurred above and below this mudstone layer. The two cavities formed in this halite facies are both of relatively uniform diameter, although the upper cavity is roughly cylindrical whilst the lower cavity tapers downwards to some extent with a broad inverted funnel shape (Figure 3, A4). The floor of the upper cavity and roof of the lower cavity are both defined by the irregularity of the dolomitic mudstone bedding surfaces.

Both the mylonite and the chicken-wire halite samples developed distinct 'compartments' or 'strongly-stepped' solution cavities during the dissolution experiment, which overall become broader in diameter downwards along the flow-path. The downward-broadening of the solution cavities in these two samples (Figure 3. A2 and A3) is notably different to the dissolution behaviour observed in the cumulate, primary founded mat and Haselgebirge facies halite samples, in which the solution cavities generally become narrower along the flow-path (Figure 3, A1, A4 and A5). The reason for the different dissolution behaviour in these two samples is not obvious. Both samples developed horizontally elongated solution cavities, although petrological analysis does not reveal any well-defined horizontal features within the fabric (e.g. microfractures, mudstone, dolomite or anhydrite

horizons, preferentially-orientated grain boundaries etc.) that might have influenced this dissolution direction (Figure 5). The chicken wire halite is highly heterogeneous, and the pronounced widening of the dissolution cavity at the base of this sample occurs in a small volume of clean halite present immediately beneath a diffuse region of particularly dirty, muddy halite. In the case of the mylonite sample the halite is quite pure, and the shape of the resulting solution cavity does not reflect the obliquely-inclined, sheared halite fabric observed within the core, indicating that the sheared fabric has exerted little influence on the overall geometry of the resulting cavity.

Comparison of X-ray CT images recorded pre- and post-experiment clearly show the extent of the dissolution post-experiment compared to the initial pilot-hole (Figure 6). The pre-experiment X-ray CT images also reveal the presence and distribution of rare to minor pre-existing natural pores within the bulk matrix of the halite samples (Figure 6A, C1 ad D1). These are generally small (typically <2 mm) and isolated. However, post-experiment X-ray CT images show that the matrix porosity in the halite adjacent to the dissolution cavities is noticeably enhanced; the number and size of apparently 'isolated' pores increasing both in abundance and size (Figure 6C and D). Volumetric measurement of this matrix porosity from the pre and post-experiment X-ray CT images for three samples (Figure 6E) shows an increase in all cases, particularly in the chicken-wire sample. This indicates that the brine creating the main dissolution cavity was also penetrating into the halite matrix locally along discrete grain boundaries or microfractures, producing minor dissolution in the matrix ahead of the advancing wall and dissolution front of the main solution cavity). Detailed X-ray CT imagery of the cumulate halite core reveals the presence of localised concentrations of these partially interconnected primary pores within sub-horizontal 'bands' of the halite matrix (Figure 7A). The development of the stepped morphology of the solution cavity in the cumulate halite can be seen to be at least partially controlled by distribution of this primary matrix porosity. Dissolution is seen to have migrated (from the central injection hole) along crystal cleavage planes in the halite matrix until it reaches an entrapped pore, where it seeds new dissolution within the void with concomitant widening of the cleavage plane. Progressive dissolution along these zones of enhanced primary porosity in the halite has led to the development of a shoulder or to stepwise widening of the main solution cavity (Figure 7A).

The extent of penetration of the reacting brine fluid during the experiment into the cavity walls was also highlighted by the distribution of the fluorescein tracer, which gave a strong response under blue-wavelength excitation as imaged by LSSFI (Figure 4). In pure halite with low matrix porosity the fluorescein largely coats the cavity surface with limited penetration into the halite in the cavity wall (e.g. the mylonite Figure 4B). In halite fabrics with higher matrix porosity, or higher mudstone content, the fluorescein has infiltrated along these discontinuities and pathways, penetrating up to 30 mm into the wallrock from the main cavity in some cases (e.g. chicken-wire, Figure 4A). Insoluble material, coated by the fluorescein, and washed out during cavity dissolution is clearly visible accumulating at the base of the cavities (e.g. primary founded mat halite, Figure 4C).

<u>Experimental set B (seawater)</u>

The experiments were run for a shorter time than the near-halite-saturated brine solution due to the faster rate of dissolution in the relatively dilute 'seawater' solution. X-ray radiography and X-ray CT imagery revealed that all dissolution cavities within the seawater experiments were remarkably similar funnel-shapes, regardless of salt fabric. (Figure 3, B1-5, Figure 7B). All fabrics have the widest part of the cavity immediately below the fluid inlet point. In both the Haselgebirge (Figure 3, B4) and the primary founded mat halite samples, (Figure 3, B5) the roof of the cavity dissolved away completely, breaching the top end of the core and creating a void between the salt and the silicon rubber under the acrylic cap of the experimental assembly. This may be due in part to failure of the sealant around the inlet tube and/or to the more aggressive nature of the dissolution in the seawater fluid. As with the brine solution experiment, the Haselgebirge sample developed two distinct cavities (Figure 3, B4) separated by a thick mudstone band (<25 mm). Despite this, the larger, uppermost cavity

still displayed the distinct funnel shape, with the lower, smaller cavity being a more cylindrical widening of the pilot hole, bounded top and base by mudstone bands.

As with the brine experiments, LSSFI under blue wavelength excitation shows that the fluorescein tracer has strongly coated the surfaces of the walls within the solution cavities. The depth of penetration of the dye into the adjacent wallrock varies between samples. The primary founded mat halite sample shows strong penetration of the fluid into the surrounding salt wallrock around the narrowest part of the dissolution cavity towards the base of the sample (Figure 4D). In the case of the chicken-wire halite, Figure 4E suggests penetration of the fluorescein has occurred preferentially on one side of the cavity, with very thin bands of the dye visible, orientated oblique to the cavity. The upper part of the cavity is also locally stained by fluorescein that has sorbed on remnants of insoluble mudstone exposed within the dissolution cavity. This is also seen in the detailed X-ray CT imagery (Figure 7B), which shows that dissolution of halite undercuts the insoluble mudstone seams and progresses up-dip beneath the mudstone seams, leaving the mudstone projecting from the wall into the cavity. In the haselgebirge facies halite Figure 4F, the surface of the upper cavity is strongly stained by the fluorescein tracer, which has also penetrated deeper into the adjacent halite wallrock along the interface between salt and two sub-horizontal, dolomitic-mudstone layers.

Petrological observations

Experimental set A (brine)

An example of some of the key petrological features observed on a cavity scale are illustrated in Figure 5, which shows details seen in thin section from the chicken-wire halite dissolution experiment with brine. Many of these features are common to all the brine experimental cavities regardless of halite fabric including: scalloping and pitting of pure halite surfaces (Figure 5A and D); localised armouring of the salt by residual insoluble mudstone, dolomite or anhydrite inclusions and layers, accompanied by undercutting of the halite beneath the insoluble component (Figure 5BC and D); cutting back and dissolution up-dip of halite beneath inclined seams of insoluble material (Figure 5D). Scallop-shaped pits or depressionsare present on the surface of all of the cavities, and X-ray CT-images show that they occur along the whole length of the cavities (e.g. Figure 6B, Figure 7A).The scallops vary from rounded hollows c.2 mm in diameter to elongated forms up to 6 mm in length. They typically display a steep surface on the 'up-flow' side and are elongated in the direction of fluid flow. They are particularly well developed in the purer salts (i.e. in the mylonite, cumulate and founded-mat halite samples, Figure 6b, Figure 7A and Figure 8A). Some protrusions of insoluble mudstone, anhydrite or dolomite were observed projecting into the cavities beyond the scalloped halite surfaces (Figure 8B). In the Haselgebirge experiment, moulds after dissolved euhedral, cubic halite crystals are preserved within the insoluble material (Figure 8C). This insoluble material was originally deposited between the halite crystals during deposition, or concentrated between halite crystals by displacive growth of halite in the muddy sediment. In other samples, insoluble material was observed to coat the surfaces of remnant pillars or projections of salt, thereby armouring and protecting the salt beneath from dissolution (Figure 8B and C), whilst the surrounding salt was dissolved away). However, these projections are vulnerable, and eventually the salt anchoring them may be breached and dissolved away, ultimately leading to the detachment of the insoluble material. This resulted in an accumulation of loose insoluble material at the base of the cavities, as seen for example in the LSSFI image of the primary founded mat experiment (Figure 4C). Where fractures existed within the sample, halite dissolution preferentially and locally focussed along these features (Figure 8D). Grain boundaries, cleavage planes and trails of fluid inclusions were also sites of preferential dissolution (Figure 9D). Although coarse-grained, fine, euhedral crystals of salt (<100 μm) are present in all fabrics. In many instances these appear to be more resistant to dissolution (Figure 9A). In this instance, the surrounding salt has begun to dissolve away, leaving the euhedral crystal intact.

Experimental set B (seawater)

In the seawater experiments, some features within the cavities are similar to those observed within the brine experiments. Scalloped pits are ubiquitous on the cavity surfaces, and in some samples (e.g. chicken-wire and mylonite) rounded scallops (<5 mm) are observed throughout the length of the cavity. As in the brine experiments, scalloping is also discernible in the sculpted salt in the cavity wall. This is particularly noticeable in the cavity roofs (Figure 9G) but X-ray CT shows that scalloping of the cavity walls occurs along the whole length of the flow path (e.g. Figure 7B). As per the brine experiments, the more insoluble sediment and anhydrite crystals stand proud of the salt cavity walls (Figures 8E-F). However, these residual features are: a) larger and more extensive (e.g. forming thin, suspended sheets of sediment bridging across the solution-etched chicken-wire cavity surfaces, e.g. Figure 8F) as also seen by X-ray CT (Figure 7B), and; b) far more delicate (Figures 8E, 8G and 9E), than those observed in the dissolution experiments using brine. Optical and SEM analysis indicate that all interstitial salt has dissolved out, leaving a delicate network of more insoluble mudstone sediment, anhydrite or dolomite crystals (Figures 9E, H). Grain boundaries have been preferentially dissolved out, which is particularly noticeable in the purer salts (Figure 9F). Where more insoluble material is present at a grain boundary, this material forms 'bridges' between the grains across the enhanced void of the grain.

Fluid measurements and geochemical analysis

The experimental leaching conditions and fluid measurements are summarised in Table 2. The progress of dissolution of the halite during the experiments was monitored by following the electrical conductivity of the discharge fluid. The electrical conductivity of the initial brine and seawater solutions were, respectively, 23.7 ±0.2 S/m and 5.43 ±0.05 S/m. The reference solution in equilibrium with pure NaCl at 22± 1 ^{o}C had an electrical conductivity of 24.9 ±0.1 S/m.

The mass loss was calculated from the difference in weight of each salt core before and after the experiments is given in Table 2. Figure 10A shows the cumulative mass loss with time of the halite samples, and the halite dissolution rate (indicated by the rate of change in chloride concentration expressed as moles Cl^- / minute) in the leachate fluid for experimental sets A and B. As expected, the dissolution rate and the cumulative mass loss over time is much greater in all the relatively-dilute seawater fluid experiments (set B) than with near-halite-saturated brine solution experiments (set A). The cumulate, haselgebirge and mylonite halites showed the least amount of dissolution during leaching with brine. In the case of the haselgebirge halite, this may be due to the halite crystals being at least partly surrounded by intercrystalline insoluble muddy sediment, which restricts access of the fluid to the soluble halite. In contrast, both the cumulate and mylonitic halite both comprise relatively pure halite. However, these two halite samples are notably coarser due to recrystallisation than the other halite types. The coarser crystal size of the cumulate and mylonitic halite would potentially give rise to less dissolution over time because the surface area of the halite crystals in contact with the reacting brine would be lower. Unlike the cumulative mass loss (Figure 10A), the halite dissolution rates, expressed in terms of rate of change of chloride concentration (Cl- / minute) during the experiments, show any obvious differences between the different halite types during either the brine-leaching experiments (Figure 10B) or seawater-leaching experiments (Figure 10C). In the brine experiments, the dissolution rates of the different halite types are broadly similar, and constant at about 0.003 moles Cl^-/minute, from the start of the experiment. With seawater, the dissolution rate increases sharply over the first 50-100 minutes but thereafter tending towards a more steady state of around 0.0035 moles Cl^-/minute over the duration of the experiments.

Figure 10D shows the conductivity of the discharging solution monitored throughout the brine (set A: primary founded mat halite only) and seawater (set B) dissolution experiments. The dissolution pattern shown by the primary founded mat with brine illustrates the typical dissolution behaviour with brine for all the halites in experiment set A. The initial brine solution (conductivity 23.7 S/m) flowing into the halite was only slightly undersaturated with respect to NaCl, and the leachate quickly reaches halite saturation within the first fluid sampling interval (i.e. within 25 minutes as shown in figure 10). For the seawater leaching experiments (set B), the leachate solutions showed a rapid increase in electrical conductivity from 5.43 S/m to values between 19-30 S/m, with a more gradual increase in salinity with elution time, achieving a steady state salinity corresponding closely to the NaCl saturation, after around 120 minute's elution time (Figure 10). Subtle differences are observed in the dissolution rate between the different halite facies before they reach steady state dissolution (refer to Figure 10): the purer primary founded mat reaches steady state dissolution much earlier (circa 75 minutes) than the other halites.

More detailed chemical analysis was carried out on the starting fluids and resulting post experimental leachates from the brine dissolution experiments: at the end of the first day; midway through, and; at the end of the experiments. Example analytical results are shown in **Error! Reference source not found.**. Other than the major cations (Na^+, K^+, Ca^{2+}) and anions (Cl^-, SO_4^{2-}), magnesium and the majority of minor and trace elements (with the exception of Sr^{2+}) are below detection. Chloride increased with time as expected, as the leaching solutions progressively dissolved the salt and approached halite saturation. Strontium also increased as the dissolution progressed and is probably attributable to the partial dissolution of anhydrite inclusions. Magnesium slightly increased with time in the cumulate sample. This might reflect liberation of Mg from exchangeable cation sites in the clay minerals (e.g. mixed-layer chlorite-smectite is known to be present in these halite formations (Plant, Jones and Haslam, 1999: Jeans, C.V. 2016)) or partial minor dissolution of dolomite. Although the Haselgebirge has a higher clay content, the clay is compact andless dispersed, and hence may be less accessible to the leaching solution. Consequently, this may account for the lack of Mg released in this experiment from the rock structure. Alkattan et al., (1997) noted that certain elements can have an inhibiting effect on salt dissolution at a constant trace metal concentration (Fe=Zn> Co> Cr> Pb> Cd), but their experiments used very high concentrations of these elements (e.g. 11597 ppm Pb) in order to monitor the effects. Although trace amounts of Pb were noted to increase up to 0.049 ppm in our experiments, the concentrations of Pb is still extremely low, and it is unlikely that it would have had any effect on dissolution.

Discussion:

The experiments performed show clear differences in the overall morphology of the dissolution cavity developed in halite, with concentration of the leaching solution (i.e. brine close to halite-saturation versus seawater). Kazemi and Jessen (1964) and Sears and Jessen (1966) demonstrated that the rate of salt removal from a cavern wall is fundamentally related to the brine concentration within the main body of the cavity. This is also reflected in our experiments, which show that the cumulative mass loss and dissolution rate with seawater is much faster than with brine (Figure 10 and Figure 11). The brine experiments (set A) showed relatively constant rates of dissolution throughout the experiment, whereas the seawater experiments (set B) showed an initial rapid increase in dissolution rate but then approached a relatively steady rate, once the leaching solution flowing through the dissolution cavity became closer to halite saturation.

One of the key findings of this study is the extent to which the salt fabric influences the resulting dissolution cavity. Final cavity morphology developed with a brine solution (experiment set A) is relatively unique for the different halite types / facies, suggesting the rock fabric is at least one of the major components influencing the halite dissolution behaviour. In contrast, leaching with a relatively dilute seawater solution produced dissolution cavities with very similar morphologies, irrespective of the halite fabric, (experimental set B) indicating little overall influence is exerted by the fabric of the salt. Much of this behaviour can be explained by considering how close the leaching solution is to halite saturation and the effect that this has on dissolution rate, compared to physical influences that the rock fabric may exert on dissolution behaviour. Empirical studies show that most mineral dissolution behaviour exhibits a sigmoidal relationship between the rate of dissolution and the degree of saturation (Arvidson and Luttge, 2010). When the system is far from equilibrium (i.e. markedly undersaturated), as with the seawater fluid, the dissolution rate will be high, and any physical differences in fabric that may affect solubility may be swamped by the overall rapid dissolution of the mineral. However, as the solution approaches mineral saturation, the reaction rate decreases sharply and reaches zero at equilibrium. Under these conditions the subtle differences in the halite fabric, such as the accessibility of the halite surfaces to the fluid, crystal size and surface area, have an increasingly important effect on dissolution rate.

Weisbrod et al. (2012) found similar shaped cavities to those in the seawater (set B) experiment formed in their flow-through experiments in halite using a pre-existing artificial channel. Using a 70% solution of Dead Sea brine, they noted massive dissolution near the solution inlet, with a dissolution volume decrease along the flow path resulting in an approximately funnel-like shaped dissolution cavity. Weisbrod et al. (2012) utilised a horizontal flow set-up in their experiments and also noted that the dissolution cavities expanded upwards relative to the initial artificial channel, suggesting that gravity and fluid density plays a key role in the dissolution behaviour. They argued that less saturated and lower density solutions, with higher dissolution potential, flow above the denser, the more saturated brine solutions, and therefore dissolution proceeded upwards in their experimental system. Although Weisbrod et al.'s (2012) experiments were carried out horizontally, similar funnel morphologies resulted from the seawater experiments in this study. However, the funnel-like morphology of the dissolution cavities in our experiments can be more simply explained by a progressive decrease in dissolution rate (and consequent reduction in halite dissolution) along the flow path as the seawater reacting with the halite becomes more saturated, eventually approaching halite saturation towards the outflow. This effect can also be seen to some extent in the brine dissolution (set A) experiments with cumulate, primary founded mat and Haselgebirge facies halites but is much more subdued. These three experiments all produced cavities that taper and diminish along the flowpath but overall were more cylindrical. In the case of the Haselgebirge halite, the development of the cavity was interrupted by a competent layer of dolomitic mudstone part-way along the flow path. Cavity development in the mylonitic and chicken-wire halite under brine solution did not follow this behaviour.

Gravity-driven density flow and the inclination and geometry of the halite surfaces were found in experiments by Durie and Jessen (1964) to significantly influence dissolution rates of salt in a saline solution. As halite dissolves a 'boundary layer' of denser water forms at the halite-water interface. Where the dissolution surface is inclined to the vertical with a positive angle ($0° \leq \theta \leq 90°$) (i.e. the water overlies the halite surface), the 'boundary layer' is continuous over the salt surface. Gravity acts to cause this denser boundary layer to flow down the slope gradient. Diffusion coefficients for NaCl in water are independent of gravitational force, so that Na and Cl ion diffusion into the boundary layer will not be affected. As the angle to the vertical (θ) increases (i.e. slope decreases), the gravity-driven flow decreases and the boundary layer becomes more halite-saturated, thereby reducing the

dissolution rate (cf. Arvidson and Luttge, 2010 and earlier discussion). Conversely, Negative angles of inclination ($90° \leq \theta \leq 0°$) have been found to produce a far greater dissolution rate than surfaces with a positive inclination, even greater than vertically inclined surfaces (Durie and Jessen 1964). In this situation, dissolution is more complex. The salinity of the water at the overlying dissolution surface increases through Na and Cl ion diffusion into the boundary layer, which becomes increasingly dense compared to the underlying solution. This situation is hydrodynamically-unstable, and therefore the denser water falls down through the less saline water. Less saline water then flows up to the dissolution surface to replace the denser solution, thereby leading to more rapid dissolution. A clear example of the effect of enhanced dissolution related to a negative angle of inclination is seen in the brine dissolution experiment with primary founded mat halite experiment from experiment set A, where the presence of an oblique insoluble mudstone layer has greatly influenced the final dissolution cavity morphology. Dissolution has preferentially extended the cavity up-dip beneath the inclined mudstone layer as denser brine resulting from the halite dissolution has flowed downwards to be displaced by fresher, less dense brine. The resulting cavity in the primary founded mat halite experiment (set A) contrasts with dissolution cavities formed in the other samples from the brine experiments, where the orientation of insoluble layers of clay or dolomite are not steeply inclined. Similar, enhanced dissolution of halite and upward-migration of the solution cavity beneath inclined insoluble mudstone laminae was also observed in the dissolution experiment with chicken-wire halite and seawater (Figure 7B).

Enhancement, or exploitation of features such as fractures, grain boundaries, and fluid inclusions by the fluid have been documented previously (e.g. Schott et al., (1989)), and are also well illustrated by the experiments in this study (e.g. Figure 9D, F, and Figure 8D). At the scale of these experiments this appears to have a strong influence on the development of the resulting dissolution cavity. X-ray CT imaging (e.g. Figure 6A and B, Figure 7A) shows an increase in the porosity within the halite matrix behind the cavity walls, particularly within the primary founded mat halite and cumulate experiments. Similarly, the “stepped” profile of the solution cavity developed in the cumulate facies halite with brine solution appears to be strongly influenced by the distribution of pre-existing partially interconnected pores or cavities in the halite. Dissolution along localised horizontal zones or arrays of these pores may be responsible for the lateral elongation of the solution cavity and development of the stepped forms seen in some of the brine dissolution experiments (e.g. Figure 7A). The origin of the pre-existing porosity in the halite is uncertain. However, the horizontal orientation of the arrays of pores in the cumulate suggests that they may be bedding-related, and could possibly represent residual brine-filled pores formed when synsedimentary porewater was trapped between consecutive layers of halite as it was being deposited. LSSFI of the distribution of the fluorescein tracer used in the dissolution experiments also shows that the leaching fluids penetrated deeper into wallrock beyond the main cavity wall, and is associated with enhancement of matrix porosity. The connecting pathways (e.g. along crystal / grain boundaries) between the visualised secondary (or enhanced) pores in the wallrock are largely below the resolution of the X-ray CT scans. Nevertheless, this is an important finding, indicating that an ‘alteration zone’ of increased matrix porosity may develop in the wallrock around the main cavity, as a precurser to cavity enlargement. This has not been observed previously, and may have some effect on the structural integrity of the cavity walls potentially weakening them. In our experiments, this extended at least 20 mm beyond the walls of the central cavity.

Recrystallised halite grains (Figure 9A) show a greater resilience to dissolution than the surrounding salt crystals. They have a lower concentration of defects and discontinuities, and are therefore dissolved at a slower rate (Meike, 1990). This is despite, insome cases, the recrystallised halite being fine grained, and since smaller grains have a greater surface area they would have been expected to dissolve at a greater rate (Schott et al., 1989, Warren 2006). The dissolution in the mylonitic halite was

559 not influenced by the steeply-inclined shear fabric preserved in the rock with either a brine or
560 seawater fluid. It was anticipated that defects and strain induced in the halite by deformation within
561 the sheared halite might have produced some degree of preferentially-orientated dissolution
562 behaviour under the near-saturated brine fluid (cf. Schott et al., 1989). However, the dissolution cavity
563 formed showed no relationship to the shear fabric. Close examination of the mylonitic halite suggests
564 that this halite largely recrystallised after deformation. Consequently, any defects or strain in the
565 halite crystals may have been removed by this process.

566 A ubiquitous feature in both the brine and seawater experiments, is the formation of scallop-shaped
567 depressions (e.g. Figure 7 and Figure 8A) on the walls of the dissolution cavities. They typically display
568 a steep surface on the 'up-flow' side and are elongated in the direction of fluid flow These features
569 were also noted by Weisbrod et al., (2012:refer to Figure 4G) along the walls of the halite dissolution
570 cavity. The development of scallop-shaped depressions on the halite dissolution surfaces is
571 characteristic of dissolution in undersaturated turbulent fluids, and similar features have also been
572 observed in limestone dissolution and ice melting (Meakin and Jamtveit, 2010). Similar scalloped
573 forms were noticeable in thin section (e.g. Figure 6D), where they occur as a result of the preferential
574 undercutting of salt behind insoluble material, which initially armours the salt and is then isolated as
575 protrusions as the salt around is dissolved away. Our observations suggest that eddy currents formed
576 in the 'lee' of these insoluble protrusions as a result of turbulent fluid flow along the halite surface.
577 Understanding the effects of turbulent flow may be an important factor to consider in the
578 development of halite solution cavities in both small-scale experiments and large-scale cavern
579 construction.

580

581 **Summary and Conclusions:**

582 One of the key findings of this study is the extent to which the salt fabric influences the resulting
583 dissolution cavity. Whilst seawater solution produced dissolution cavities with similar morphologies,
584 brine dissolution cavities developed with morphologies that were relatively unique for the different
585 halite facies, suggesting rock fabric is at least one of the major components influencing the halite
586 dissolution behaviour. Much of this behaviour can be explained by considering how close the leaching
587 solution is to halite saturation, and therefore the effect on dissolution rate. As the solution approaches
588 mineral saturation, the reaction rate decreases sharply, reaching zero at equilibrium. Therefore under
589 these conditions, subtle differences in halite fabric have an increasingly important effect on
590 dissolution rate.

591 Enhancement or exploitation of features within the halite, such as fluid inclusions and grain
592 boundaries, by the fluid are well illustrated by this study. X-ray CT imaging reveals an increase in the
593 porosity within the halite matrix beyond the cavity walls, particularly within the primary founded mat
594 halite and cumulate experiments. LSSFI of the distribution of the fluorescein tracer used in the
595 dissolution experiments also shows that the leaching fluid penetrates deep into the halite matrix
596 beyond the main cavity walls and is also associated with the enhancement of matrix porosity. The
597 resolution of the X-ray CT scans is below the connecting pathways (e.g. along crystal / grain
598 boundaries) between the visualised secondary (or enhanced) pores in the wallrock. Nevertheless, this
599 is a key finding, not previously observed, indicating that a 360^{o} 'alteration zone' of increased matrix
600 porosity develops around the main cavity, as a precurser to cavity enlargement. This may have some
601 effect on the structural integrity of the cavity walls potentially weakening them. In our small-scale
602 experiments, this enhanced dissolution extended at least 20 mm beyond the walls of the central
603 cavity.

The formation of scallop-shaped depressions was found to be a ubiquitous feature on the walls of the dissolution cavities in both types of experiment. We suggest these are the result of eddy currents forming in the 'lee' of insoluble protusions as a result of turbulent fluid flow along the halite surface.

In the development of halite solution cavities in both small-scale experiments and large-scale cavern construction, understanding the effects of this turbulent flow may be an important factor to consider.

Acknowledgements:

This paper is dedicated to Aurelie Devez, who sadly passed away in 2017. A number of BGS colleagues are thanked for their assistance during the work: Edward Hough for discussion and guidance on the halite core samples and fabrics developed therein, John Fletcher and Simon Harris for the thin sections and the 3D laser-scanning of the half cores, respectively, and Daniel Parkes who assisted with the monitoring of some experiments. X-ray radiography was carried out by Andrew Saunders and Michael Mills of Intertek NDT Services Ltd, Derby, UK. This paper is published with the permission of the Executive Director of the British Geological Survey (NERC).

Funding Information:

This work was funded under the EPSRC Integrated Market-Fit Affordable Grid-Scale Energy Storage (IMAGES) project, grant code EP/K002228/1.

References:

Alkattan, M., Oelkers, E.H., Dandur J. L., and, and Schott, J. (1997), Experimental studies of halite dissolution kinetics. 1. The effect of saturation state and the presence of trace metals, Chemical Geology, 137: 201–219, doi:10.1016/S0009-2541(96)00164-7.

Arthurton, R.S. 1973. Experimentally produced halite compared with Triassic layered halite-rock from Cheshire, England. Sedimentology 20: 145-160

Arvidson, R.S., Luttge, A. 2010, Mineral dissolution kinetics as a function of distance from equilibrium. New experimental results. In: A special Tribute to Tim Drever. (Stillings, L.L., Poulson, S., Eds.), Chemical Geology, 269: 79-88.

Bates, R.L. and Jackson, J.A. 1987. Glossary of Geology, 3rd Ed., American Geological Institute, Alexandria, Virginia.

Bein, A., Hovorka, S., and Fisher, R.S., and Roedder, E. 1991. Fluid inclusions in bedded Permian halite, Palo Duro basin, Texas: Evidence for modification of seawater in evaporite brine-pools and subsequent early diagenesis. Journal of Sedimentary Petrology 61(1): 1-14.

BS 1998. BS EN 1918-3: Gas Supply Systems – Underground gas storage – Part 3. Functional recommendations for storage in solution-mined caverns. British Standards Institution, London.

Carter, N.L., Horseman, S.T., Russell, J.E., and Handin, J. 1993. Rheology of rock salt. Journal of Structural Geology, 15: 1257 – 1271.

Charnavel. Y. 2012. Illustration case in bedded salt: Stublach Gas Storage Project: Fundamentals of Salt Cavern Development. Solution Mining Research Institute (SMRI) Fall 2012 Bremen, Germany, Technical Class, 30 September 2012, 19 pp.

Charnavel. Y., O'Donnell, J. and Ryckelynck, T. 2015. Solution mining at Stublach. Solution Mining Research Institute (SMRI) Spring 2015 Technical Conference, Rochester, New York, 27-28 April, 14 pp.

Crotogino, F., Mohmeyer, K-U., and Scharf, R. 2001. Huntorf CAES: More than 20 years of successful operation. Spring 2001 Meeting, Orlando, Florida, USA, 15-18th April 2001. (AKE2003H03c_Crotogino_ea_HuntorfCAES_CompressedAirEnergyStorage.pdf).

Crotogino, F. and Huebner, S. 2008. Energy Storage in Salt Caverns: Developments and Concrete Projects for Adiabatic Compressed Air and for Hydrogen Storage. Solution Mining Research Institute Spring 2008 Technical Conference, Porto, Portugal, April 28–29, 2008.

Currey, P. 2012. At the energy crossroads: Technology Ventures scouts uncharted terrain. ConocoPhillips spirit Magazine, second quarter 2012 edition, 52 pp. http://www.conocophillips.com/who-we-are/Spirit%20Magazine/2qtr12_spiritmag.pdf

Durie, R.W. and Jessen, F.W. 1964. The influence of surface features in the salt dissolution process. Society of Petroleum Engineers Journal, 4, 275-281.

Evans, D.J. 2007. An appraisal of Underground Gas Storage technologies and incidents, for the development of risk assessment methodology. British Geological Survey Open Report, **OR/07/023**. 287pp. http://nora.nerc.ac.uk/7877/1/OR07023_Vol_1.pdf

Evans, D.J. 2016. Review of UK underground natural gas, LPG and proposed compressed air storage facilities - location and operational parameters. British Geological Survey Commercial in Confidence report, CR/16/197, 98 pp.

Evans, D.J. and Holloway, S. 2009. A review of onshore UK salt deposits and their potential for underground gas storage. Geological Society, London, Special Publications v313, pp. 39-80. DOI: 10.1144/SP313.5

Fokker, P.A., Steeneken, P.V. and Kruse, G.A.M. 2000. Predictable and Manageable Subsidence above Deep Salt Mining. Solution Mining Research Institute, Fall Meeting, San Antonio, 8 pp.

Gaelectric. 2015. Gaelectric energy storage: The missing link. Company newsletter available on line. Accessed November 14th 2015. http://www.gaelectric.ie/wpx/wp-content/uploads/2015/09/Gaelectric-Supplement-June-2015.pdf

Geluk, M.C., Paar, W.A. and Fokker, P.A. 2007. Salt. In: Wong, Th.E., Batjes, D.A.J. and Jager de, J. (editors), Geology of the Netherlands. Royal Netherlands Academy of Arts and Sciences, 283–294.

George, B., Laporte, P. and Richner, D. 1974. History of Solution Mining at Hauterives, France. Fourth International Symposium on Salt, Northern Ohio Geological Society, Salt Institute, 239-249.

Goodman, J.O. 1992. History of the first U.S. Compressed Air Energy Storage (CAES) Plant (110-MW-26h), Volume 1: Early CAES development. Report produced by the Electrical Power Research Institute (EPRI), Project 2894-01 Volume 1, Final Report, EPRI TR-101751, December 1992, 150 pp.

Hickman, S.H. and Evans, B. 1995a. Kinetics of pressure solution at halite-silica interfaces and intergranular clay films. 1995. USGS Staff – Published Research Paper, 411.

Hickman, S.H. and Evans, B. 1995b. Kinetics of pressure solution at halite-silica interfaces and intergranular clay films. 1995. Journal of Geophysical Research: Solid Earth, 100 (B7), 13113-13132.

Hough, E., Evans, D.J. and Williamson, J.P. 2011. A geological reappraisal of the Preesall Saltfield, Lancashire, United Kingdom: recognizing geological factors relevant to gas storage. SMRI 2011 Technical Conference, Fall Meeting, 3–4 October 2011, York, United Kingdom, 21 pp.

685 Jeans, C.V., 2016. Clay mineralogy of the Permo-Triassic strata of the British Isles: onshore and
686 offshore. Clay Minerals, 41(1), 309-354 DOI: https://doi.org/10.1180/0009855064110199.

687 Kazemi, H., and Jessen, F. W. (1964). Mechanism of flow and controlled dissolution of salt in solution
688 mining. Society of Petroleum Engineers Journal, 4(04), 317-328.

689 Kupfer, D.H. 1990, Anomalous features in the Five Island salt stocks, Louisiana. Transactions Gulf Coast
690 Association of Geological Societies, 40, 425-437.

691 Leith, W. 2001. Geologic and Engineering Constraints on the Feasibility of Clandestine Nuclear Testing
692 by Decoupling in Large Underground Caverns. U.S. Geological Survey Open File Report, 01-28, 56pp
693 (This report can be downloaded from the USGS Eastern Region Publications web site:
694 http://geology.usgs.gov/open-file/2001.html or the USGS Eastern Region Earth Surface Processes
695 Publications web site: http://geology.er.usgs.gov/eespteam/EESPT_PUB.html).

696 Looff, K.M. and Rautman, C. 2010a. Inferring the geologic significance and potential impact of salt
697 fabric and anomalous salt on the development and long term operation of salt storage caverns on Gulf
698 Cost salt domes. Solution Mining Research Institute Spring Meeting Technical Conference, Grand
699 junction, Colorado, USA, 26-27 April 2010.

700 Looff, K.M. and Rautman, C. 2010b. Salt spines, boundary shear zones and anomalous salts: their
701 characteristics, detection and influence on salt dome storage caverns. Solution Mining Research
702 Institute Spring Meeting Technical Conference, Grand junction, Colorado, USA, 26-27 April 2010, 23pp.

703 Lord, A.S. 2009. Overview of geologic storage of natural gas with an emphasis on assessing the
704 feasibility of storing hydrogen. Sandia Report, SAND2009-5878, 28pp.

705 Meike, A. 1990. A micromechanical perspective on the role of dislocations in selective dissolution.
706 GeochemIca et Cosmochimica Acta, 54: 3347-3352

707 Meakin, P. and Jamtveit, B. 2010. Geological pattern formation by growth and dissolution in aqueous
708 systems. Proceedings of the Royal Society A, **466**, 659-694.

709 Plant, J.A., Jones, D.G. Haslam, H.W. editors (1999) The Cheshire Basin: basin evolution, fluid
710 movement and mineral resources in a Permo-Triassic rift setting. British Geological Survey.
711 Nottingham. ISBN 0852723334 9780852723333

712 Raeside, R. 2003. Fluid Inclusions Analysis and Interpretation. Mineralogical Association of Canada,
713 Vancover, British Columbia,.

714 Roedder, E. 1984. "The fluids in salt." American Mineralogist, 69: 413 - 439.

715 Sears, G. F., and Jessen, F. W. 1966. Controlled solution mining in massive salt. Society of Petroleum
716 Engineers Journal, 6(02): 115-125.

717 Schott J., Brantley S., Crerar D., Guy C., Borcsik M., and Williame C. 1989. Dissolution kinetics of
718 strained calcite. Geochimica et Cosmochimica, 53: 373–382.

719 Spötl, C. 1989. The Alpine Haselgebirge formation, northern calcareous Alps (Austria): Permo-
720 Scythaian evaporates in an alpine thrust system. Sedimentary Geology, 65: 113-125.

721 Tucker, M.E. 2001. Sedimentary Petrology: An Introduction to the Origin of Sedimentary Rocks. 3rd
722 Edition p170. Blackwell Publishing, Oxford.

723 Warrington, G., Wilson, A.A., Jones, N.S., Young, S.R. and Haslam H.W. 1999. Chapter 2: Statigraphy
724 and sedimentology. In: Plant, J.A., Jones, D.G. and Haslam, H.W. The Cheshire Basin: Basin Evolution,
725 Fluid Movement and Mineral Resources in a Permo-Triassic Rift Setting. British Geological Survey,
726 Nottingham, United Kingdom, 10-40.

727 Warren, J.K. 2006. Evaporites: Sediments, Resources and Hydrocarbons. Springer-Verlag, Berlin, 1035
728 pp.

729 Weisbrod, N., Alon-Mordish, C., Konen, E., and Yechieli, Y. (2012) Dynamic dissolution of halite rock
730 during flow of diluted saline solutions. Geophysics Research Letters, 39: L09404.
731 doi:10.1029/2012GL051306

732 Wilson, A.A. and Evans, W.B. 1990. Geology of the country around Blackpool. British Geological Survey
733 Memoir, England and Wales. Sheet 66, HMSO, London.

734 Wilson, A.A. 1993. The Mercia Mudstone Group (Trias) of the Cheshire Basin. Proceedings of the
735 Yorkshire Geological Society, 49, 171-188.

736

737 **Figure captions:**

738 **Figure 1**

739 The five end-member salt facies fabrics used for the experiments in sets A and B. A) Primary founded
740 mat. B) Halite cumulate. C) Mylonite. D) Chicken wire. E) Haselgebirge.

741 **Figure 2**

742 Experimental set up. A) Schematic of the experimental set-up. The brine flow through was designed
743 to flow from top down to mimic full scale cavern dissolution. B) A photograph of the experimental set
744 up in operation. C) An example of the capped experimental salt core blocks.

745 **Figure 3**

746 Comparison between the cavities (outlined in red for clarity) resulting from experiment set A (brine)
747 and experiment set B (seawater) experiments in each of the salt end-member fabrics. All images are
748 x-ray radiography images taken of the unsampled cores, post-experiment, except image A5 which is a
749 photograph of the cavity following the halving of the post-experimental core. The directional arrows
750 denote direction of experimental fluid flow. The dissolution cavities in B4 and B5 completely dissolved
751 the roof of the salt beneath the acrylic caps.

752 **Figure 4**

753 Combined red-blue wavelength image examples derived from post-experiment laser-simulated
754 fluorescence scanning. The yellow and green colour within the images reflect clay and organic material
755 within the salt (red wavelength), whereas the red reflects the location of the fluorescein (blue
756 wavelength). Images from experimental set A. A) Chicken wire halite– the fluorescein has penetrated
757 oblique pathways (microfractures) either side of the cavity. B) Mylonite halite – the fluorescein is
758 contained within the cavity bounds. C) Primary founded mat halite – the strong band of clay and
759 organic material that controls the upper boundary of the cavity, is clearly shown by the green and
760 yellow colouration derived from the red wavelength. The fluorescein is concentrated within the
761 material on the roof of the cavity, and in the debris at the base. Images from experimental set B. D)
762 primary founded mat halite – there is a marked area at the base of the funnel where the fluorescein
763 has penetrated into the host rock side of the dissolution cavity. E) Chicken wire halite – there is marked
764 penetration by the fluorescein around the cavity. The marked red line around the outer edge of the
765 sample is due to a sticky tape around the outer edge of the sample which fluoresces within the blue
766 wavelength. F) Haselgebirge the upper cavity shows strong fluorescein presence; this is probably due

767 in part to the fluorescein coating the insoluble material within the cavity. Again this sample was taped
768 around the outer edge for cohesion following cutting.

769 **Figure 5**

770 Optical mages from the polished thin section showing example key features in the dissolution cavity
771 produced from chicken-wire halite dissolved with brine solution. Centre: scanned image of the two
772 large format polished thin section showing the whole cavity. A) Detail in pure halite of where
773 scalloping is being initiated in the vertical walls of the cavity. B) Seam of insoluble material mudstone
774 and anhydrite, locally armouring the surface with dissolution undercutting the halite beneath. C) A
775 seam of insoluble material on either side of which the halite is being preferentially dissolved. D)
776 Distinct small scale scalloping and upward migration of cutting-back up-dip on the roof of the broad
777 compartment at the base. This contrasts with the smooth curve of the floor of this compartment.

778

779 **Figure 6**

780 Example X-ray CT images of pre- and post-dissolution halite experimental cores. A) The 4 mm pilot
781 hole from the primary founded mat halite. B) Post-experiment (brine) cavity developed in the primary
782 founded mat halite (note: not to the same scale as A). C1 and C2 are planar views, identically scaled,
783 of the original pilot hole and the resulting cavity for same sample (note: the scaling has resulted slight
784 cropping of the outer limits of the scan for the post-experimental cavity to remove edge effects from
785 the outer core wall). D1 and D2 are as C1 and C2 for the "chicken-wire" halite. Note the increase in
786 porosity in the host rock, away from the post-experimental cavity in both examples. E) Histogram
787 showing the calculated change in closed pore volume in μm^3, (i.e. pore space excluding the pilot hole
788 and post-experimental cavity).

Figure 7

A) X-ray CT image of the external surface of the dissolution cavity created by the brine solution in cumulate halite. The image shows that the walls of the cavity are 'stepped' where the dissolution appears to preferentially progress along localised trails of interconnected pores or microcavities in the halite wallrock (X-X). The surface of the cavity displays well-developed 'scallop-marks'. B) X-ray CT image of the internal surface of the funnel-shaped dissolution cavity created by the seawater solution in chicken wire halite superimposed on the X-ray CT image of the original pre-dissolution pilot hole (p). The image has been false-coloured to highlight the irregular and discontinuous thin mudstone seams (red-orange), differentiated from halite by their difference X-ray density (absorbance). Dissolution can be seen to have under-cut and progressed up-dip beneath the insoluble mudstone seams (m) exposed in the cavity wall, leaving them projecting into the open cavity. The surface of the cavity displays well-developed 'scallop marks' due to turbulent fluid flow along the cavity walls.

Figure 8

Optical binocular microscope photographs showing some of the key dissolution features on the halite solution cavity surfaces. A-D are from experiment set A (brine). E-H are from experiment set B (seawater). A) Strong scalloping (mylonite halite). B) An example of insoluble remnants of material (chicken wire). C) Insoluble material defining euhedral halite moulds where halite has been dissolved away (haselgebirge halite). D) Dissolution exploiting a fracture within the salt (haselgebirge halite). E) Delicate microporous projection of insoluble sediment material (primary founded mat halite). F) Sheets of intact insoluble material (chicken wire halite). G) Networks of insoluble material standing proud across the halite surface (haselgebirge halite). H) Delicate structures of insoluble material where the salt has been completely dissolved out (haselgebirge halite).

Figure 9

Secondary electron SEM images showing some of the key dissolution features on the halite solution cavity surfaces. A-D are from experiment set A (brine). E-H are from experiment set B (seawater). A) Recrystallised euhedral halite has a density contrast to the surrounding salt which is being preferentially dissolved (mylonite halite). B and C) armouring of the salt by more insoluble material (anhydrites and clays: primary founded mat halite). D) Most samples show evidence of preferential grain-boundary dissolution. This example is from the cumulate. E) Delicate projection of insoluble material (mylonite halite). F) A preferentially dissolved grain boundary. Note the bridges across the boundary formed from remnant insoluble clay and anhydrite material (mylonite halite). G) Delicate scalloped sculpted salt (chicken wire halite). H) Detail of the insoluble material showing that all salt has been completely dissolved out, leaving a delicate network of anhydrite and clay material (chicken wire halite).

Figure 10

Weight loss, dissolution rate and conductivity over time: A) Total weight loss: brine and seawater (Experiment sets A and B); B) Salt dissolution rate for Experiment set A (brine); C) Salt dissolution rate for Experiment set B (seawater). D) Conductivity over time for experimental set B seawater solutions. A typical result from the brine experimental set A (primary founded mat) is shown for comparison.

Table 1

Click here to download Table Table 1.xlsx

Table 1 - Experimental samples

Borehole	Formation	Location	Texture*	Experiment A (brine)	Experiment B Seawater
Arm Hill	Preesall Halite	Lancashire	M		x
Arm Hill	Preesall Halite	Lancashire	M	x	
Arm Hill	Preesall Halite	Lancashire	PFM	x	
Arm Hill	Preesall Halite	Lancashire	PFM		x
Arm Hill	Preesall Halite	Lancashire	CW	x	
Arm Hill	Preesall Halite	Lancashire	CW		x
Northwich	Cheshire Northwich	Cheshire basin	C	x	
Northwich	Cheshire Northwich	Cheshire basin	C		x
Northwich	Cheshire Northwich	Cheshire basin	H	x	
Northwich	Cheshire Northwich	Cheshire basin	H		x

**M = mylonite, PFM = primary founded mat, CW = chicken wire, C = cumulate, H = Haselgebirge*

Table 2

Table 2 Summary of the experimental leaching conditions and measurements of the discharging fluid

		Inlet solution type*	Cumulative duration of discharging fluid (min)	Average temp °C	Average conductivity (S/m)	Mass loss rate (g/l eluent)
Mylonite	Day 1	**brine**	447	23	25.0	23
	Day 2		972	23	24.9	n.d.†
	Day 3		1377	24	25.2	30
	Day 4		1812	23	25.0	14
		seawater	655	22.9	23.6 - 24.6	291
Primary founded mat	Day 1	**brine**	242	23	25.0	12
	Day 2		734	23	25.0	47
	Day 3		1350	23	25.0	42
	Day 4		1801	23	25.2	46
	Day 5		2297	23	25.2	47
	Day 6		2532	23	25.2	50
		seawater	335	23	24.2	690
Chicken wire	Day 1	**brine**	192	22	n.d.	65
	Day 2		627	22	n.d.	24
	Day 3		1211	22	n.d.	27
	Day 4		1720	22	n.d.	26
	Day 5		2227	22	n.d.	27
	Day 6		2458	22	n.d.	36
		seawater	307	22.3	23.8	249
Cumulate	Day 1	**brine**	436	22	n.d.	31
	Day 2		877	23	n.d.	36
	Day 3		1205	22	n.d.	46
	Day 4		1514	23	n.d.	54
		seawater	315	22.9	23.6	267
Haselgebirge	Day 1	**brine**	606	22	n.d.	28
	Day 2		1224	22	n.d.	16
	Day 3		1686	22	n.d.	14
	Day 4		2192	22	n.d.	16
		seawater	315	22.9	23.5	245

*All experiments conducted at a constant flow rate: 540 mm3/min
n.d. - no data
n.d.† - no data for day 2 as sample required resealing

Table 3

Click here to download Table Table 3.xlsx

Table 3 Example geochemical data:

	Brine (Exp set A)	Ca mg l^{-1}	Mg mg l^{-1}	Na mg l^{-1}	K mg l^{-1}	Cl- mg l^{-1}	Total S mg l^{-1}	Sr µg l^{-1}	Cu µg l^{-1}	Rb µg l^{-1}
	ICP-MS Detection limit (DL)	**156**	**4**	**38**	**10**		**312**	**23**	**17**	**4**
Cumulate	**625A**									
	Starting brine 270 g/l NaCl	<156	<4	97300	<10	171143	<312	<23	<17	<4
	Leachate day 1	<156	6	115342	13	174967	<312	93	<17	<4
	Leachate day 2 (with fluorescene)	<156	12	120626	13	179447	<312	303	<17	<4
	Leachate day 4 (with fluorescene)	<156	15	115066	13	184845	<312	465	18	<4
Haselgebirge	**626A**									
	Starting brine 270 g/l NaCl	<156	<4	106590	<10	159575	<312	<23	<17	<4
	Leachate day 1	163	<4	105689	20	166153	<312	200	25	14
	Leachate day 2 (no fluorescene)	203	<4	115752	15	181374	340	237	17	6
	Leachate day 4 (no fluorescene)	247	<4	122465	18	185587	<312	876	<17	12

Elements below detection limits: Si, Mn, Fe, Li, Be, B, Al, Ti, V, Cr, Co, Ni, Zn, Ga, As, Se, Y, Zr, Nb, Ag, Sn, Sb, La, Ce, Pr, Nd, Sm, Eu, Th, U

Mo µg l^{-1}	Cd µg l^{-1}	Cs µg l^{-1}	Pb µg l^{-1}
6	**4**	**2**	**5**
6	<4	<2	10
<6	<4	<2	<5
<6	<4	<2	49
<6	5	<2	7
14	4	<2	<5
14	6	2	45
8	<4	<2	11
9	<4	<2	22

, Gd, Tb, Dy, Ho, Er, Tm, Yb, Lu, Hf, Ta, W, Ti,

Figure 1

Click here to download Figure Fig 1.png

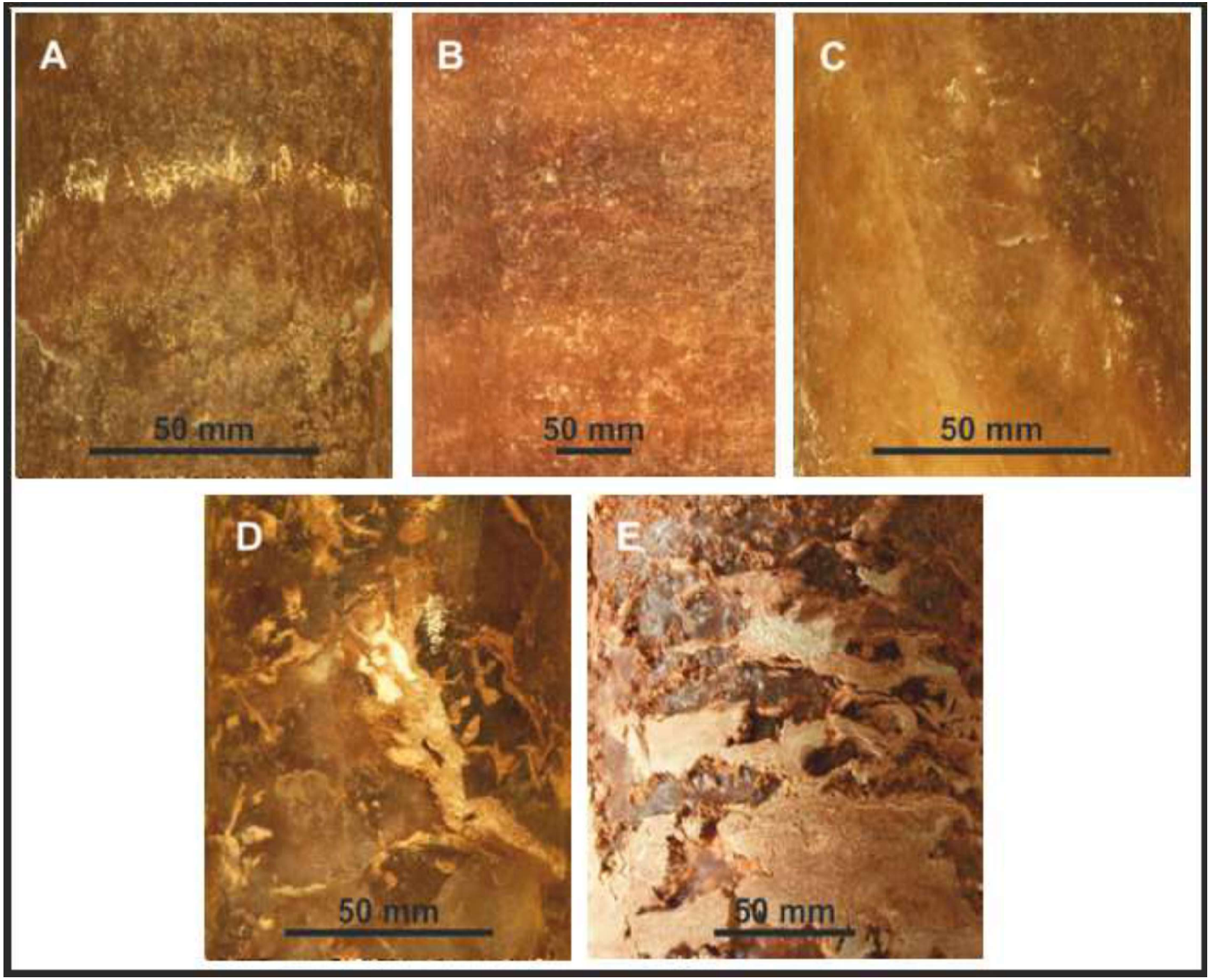

Figure 2

Click here to download Figure Fig 2.png

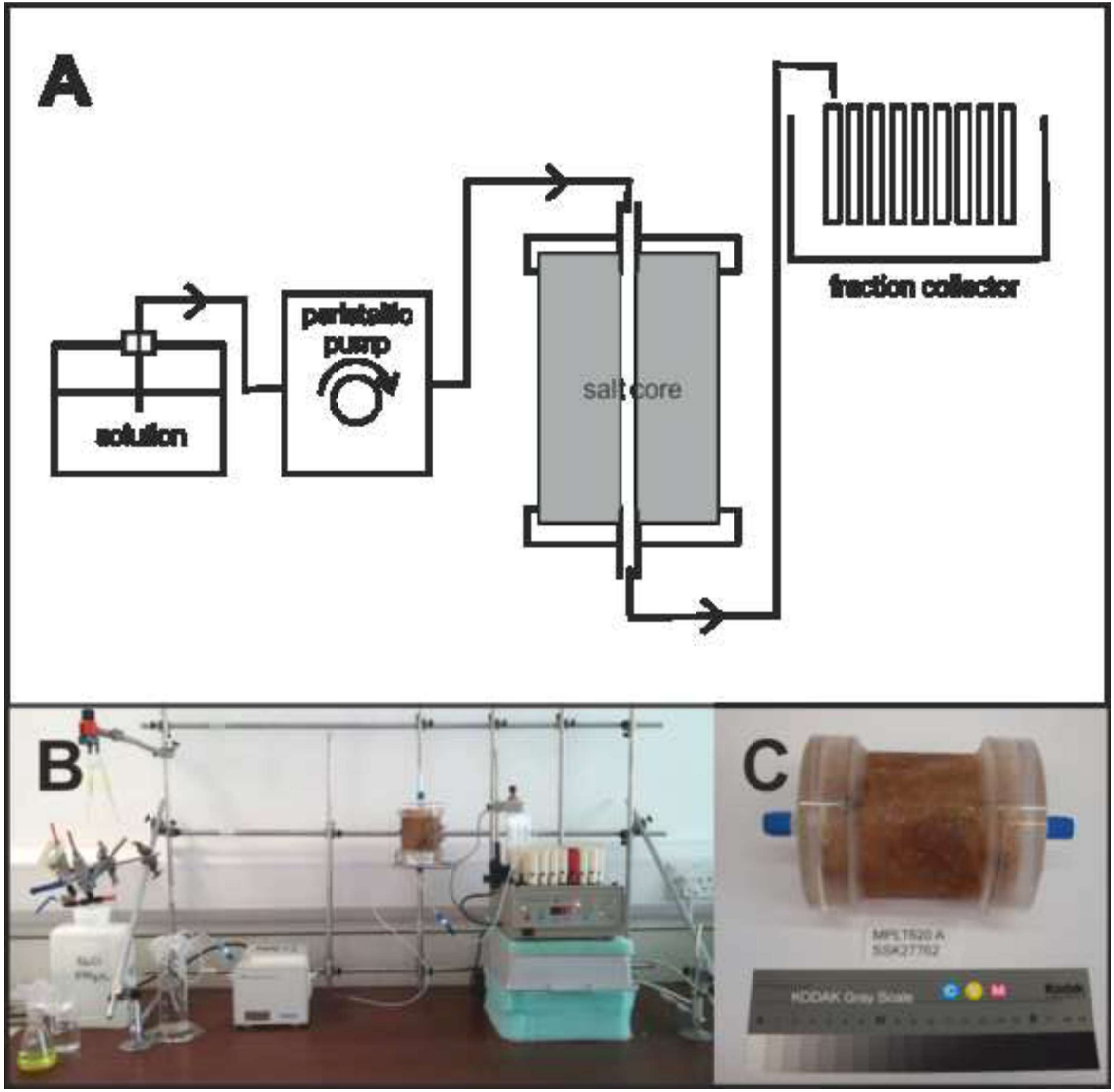

Figure 3

Click here to download Figure Fig 3.png

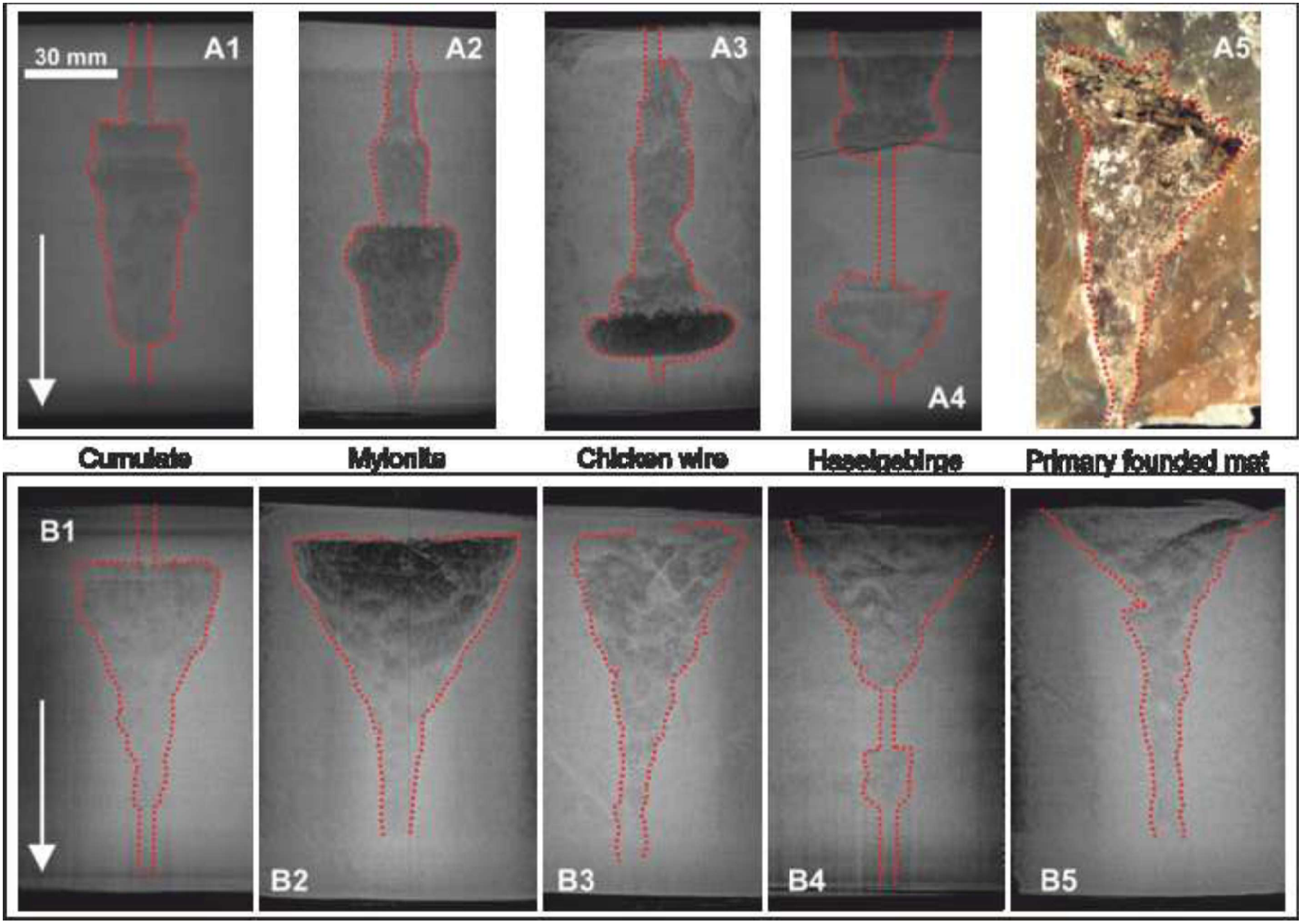

Figure 4

Click here to download Figure Fig 4.png

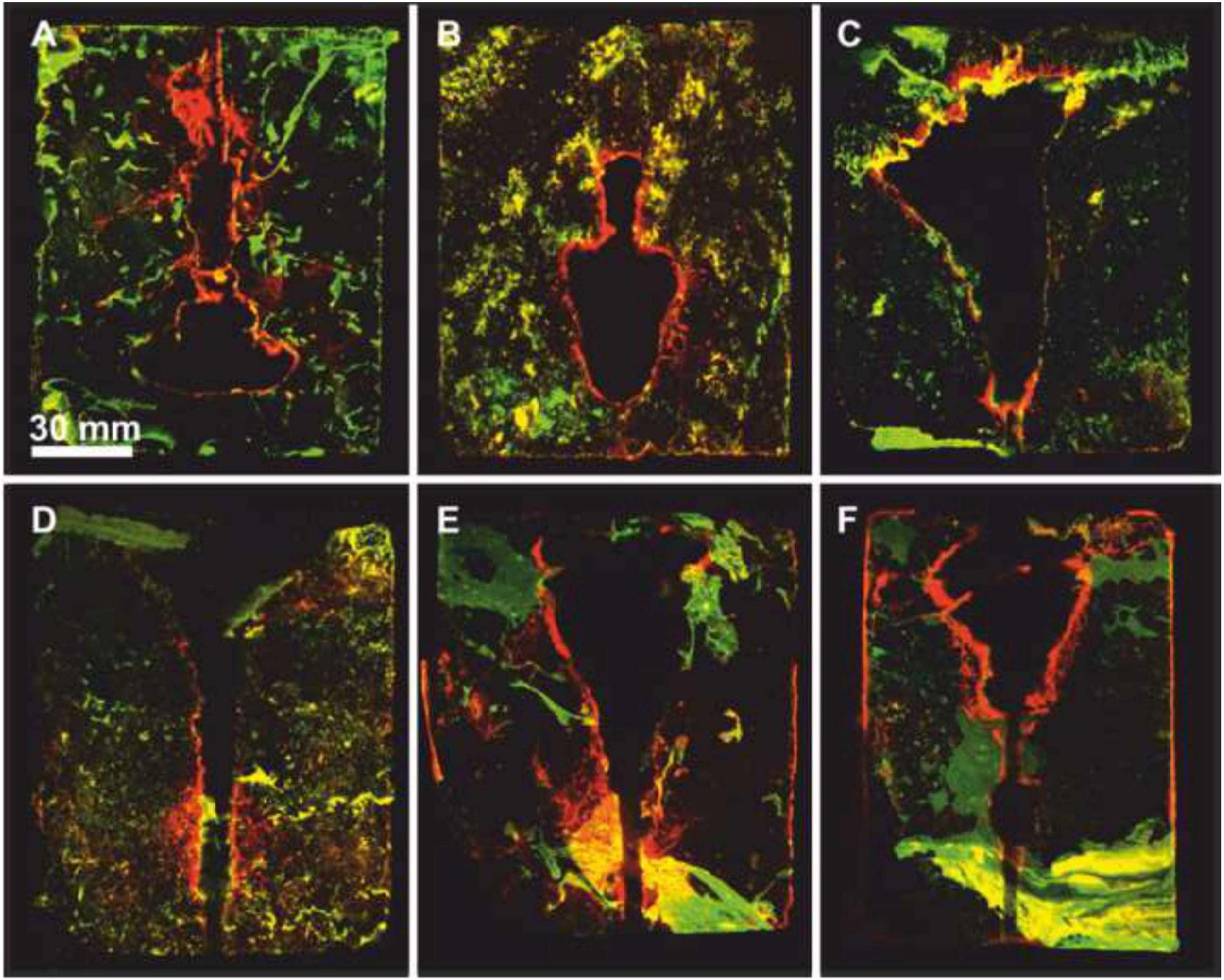

Figure 5

Click here to download Figure Fig 5.png

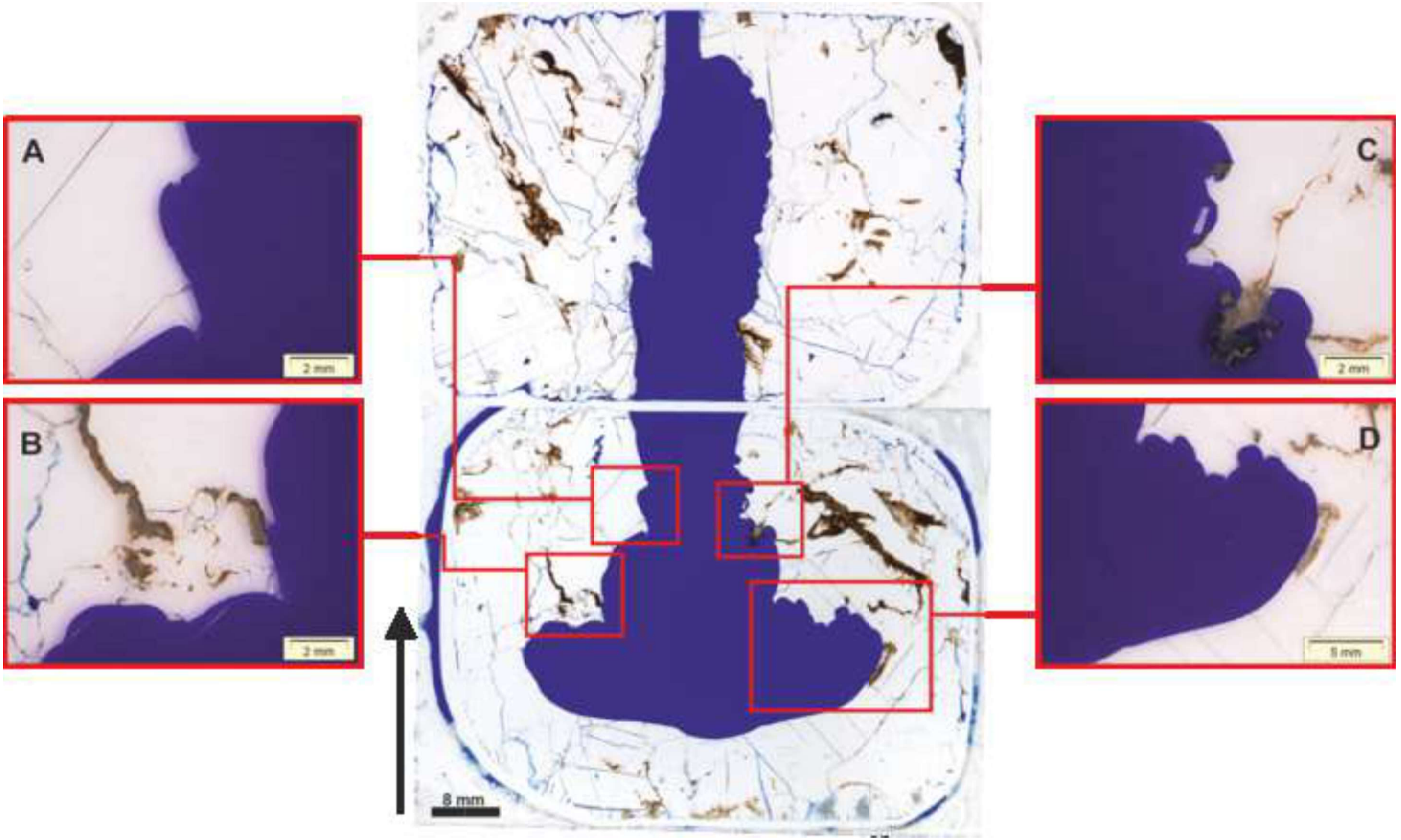

Figure 6

Click here to download Figure Fig 6.png

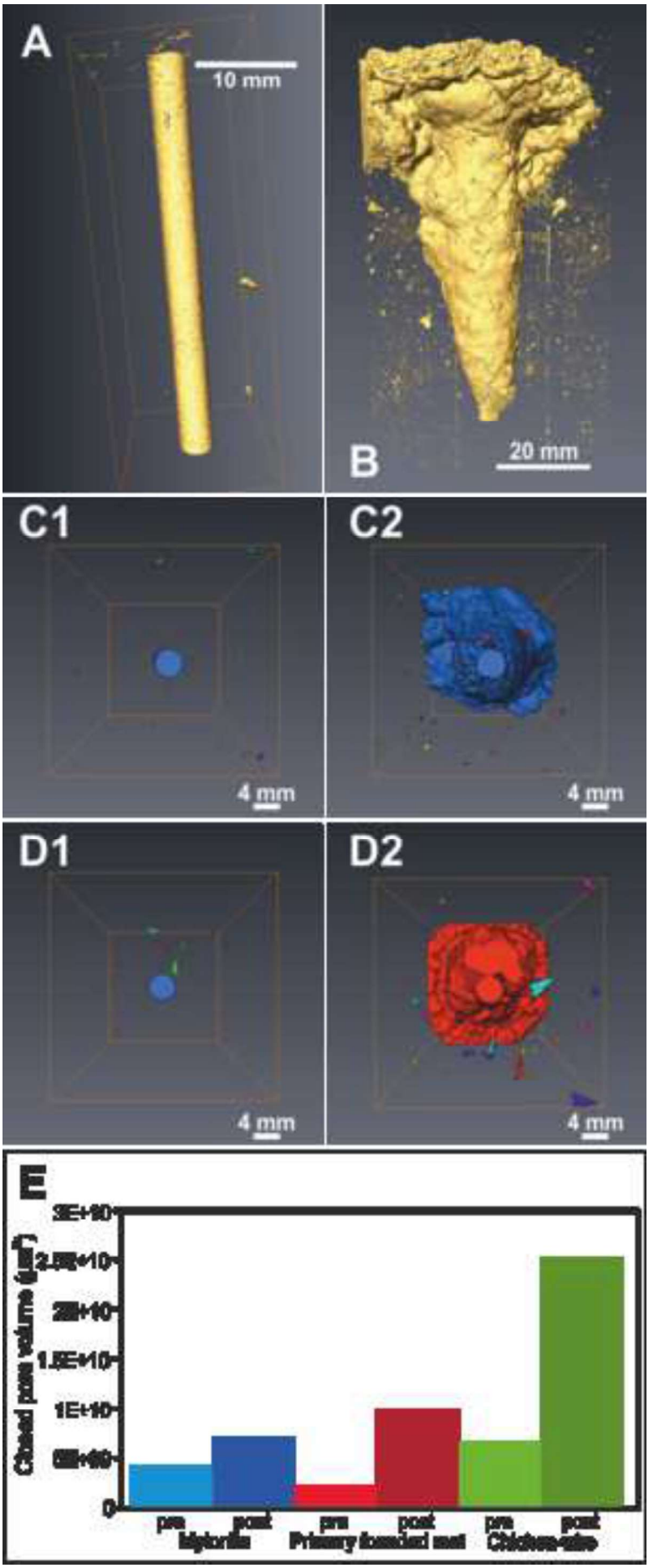

Figure 7

Click here to download Figure Fig 7.png

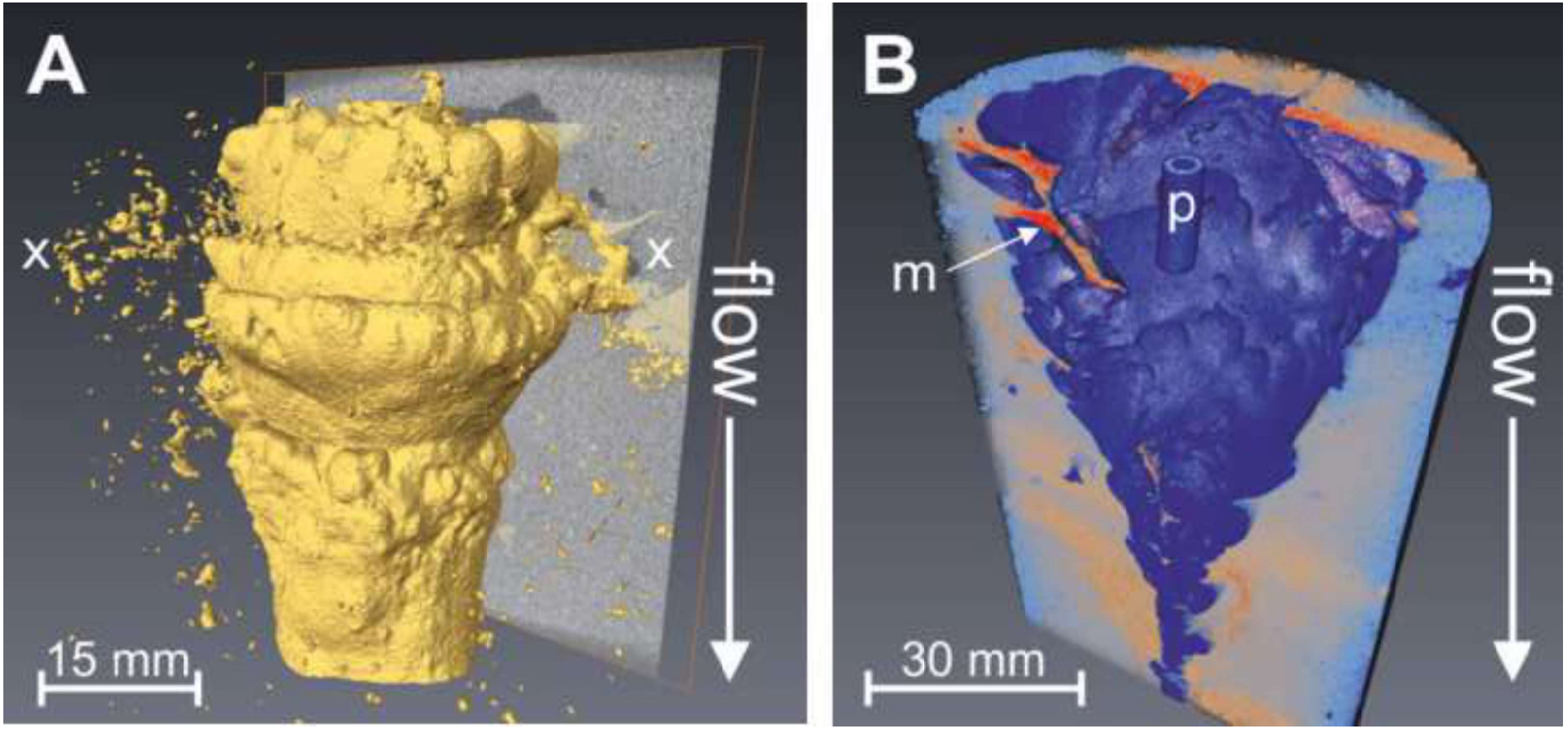

Figure 8

Click here to download Figure Fig 8.png

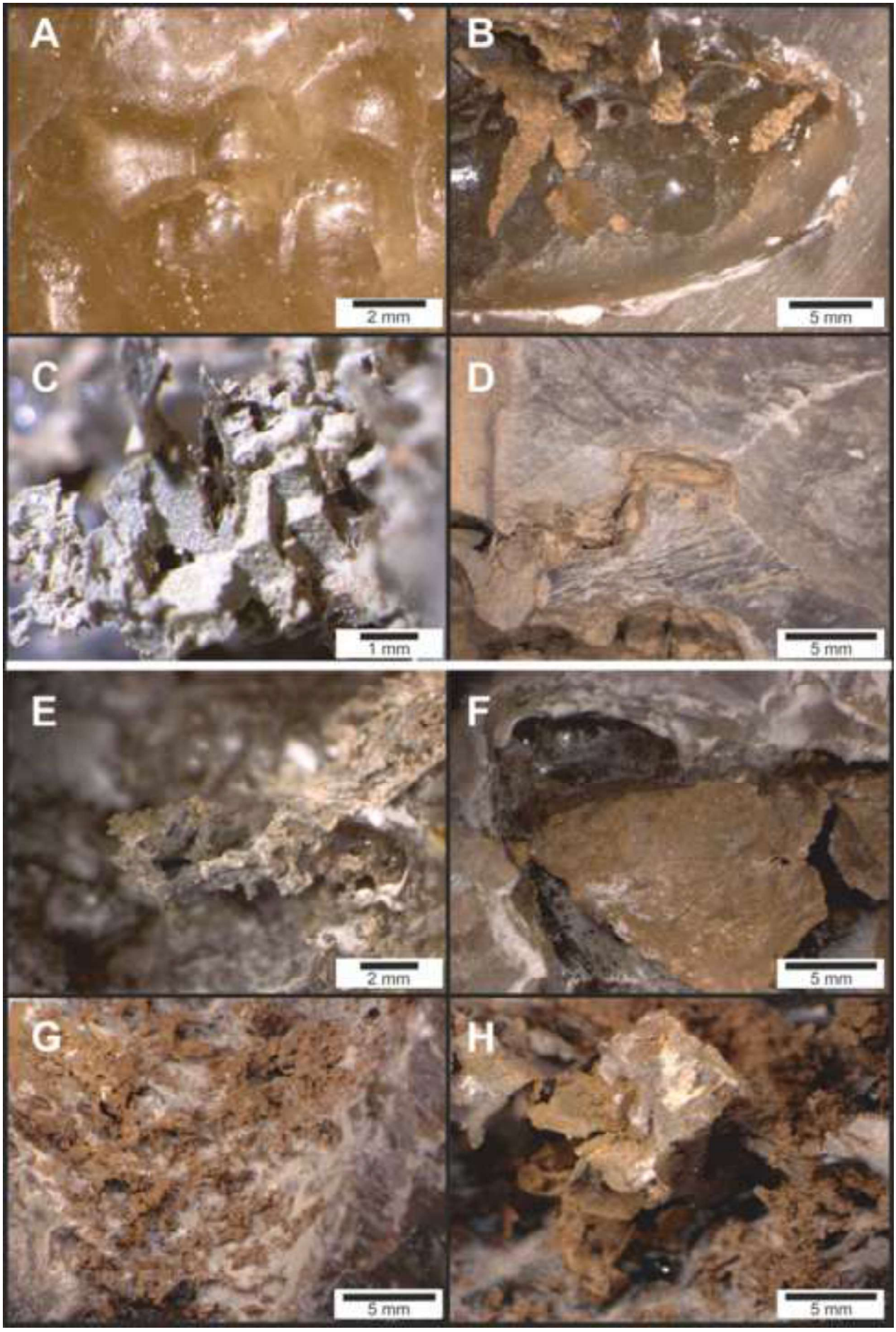

Figure 9

Click here to download Figure Fig 9.png

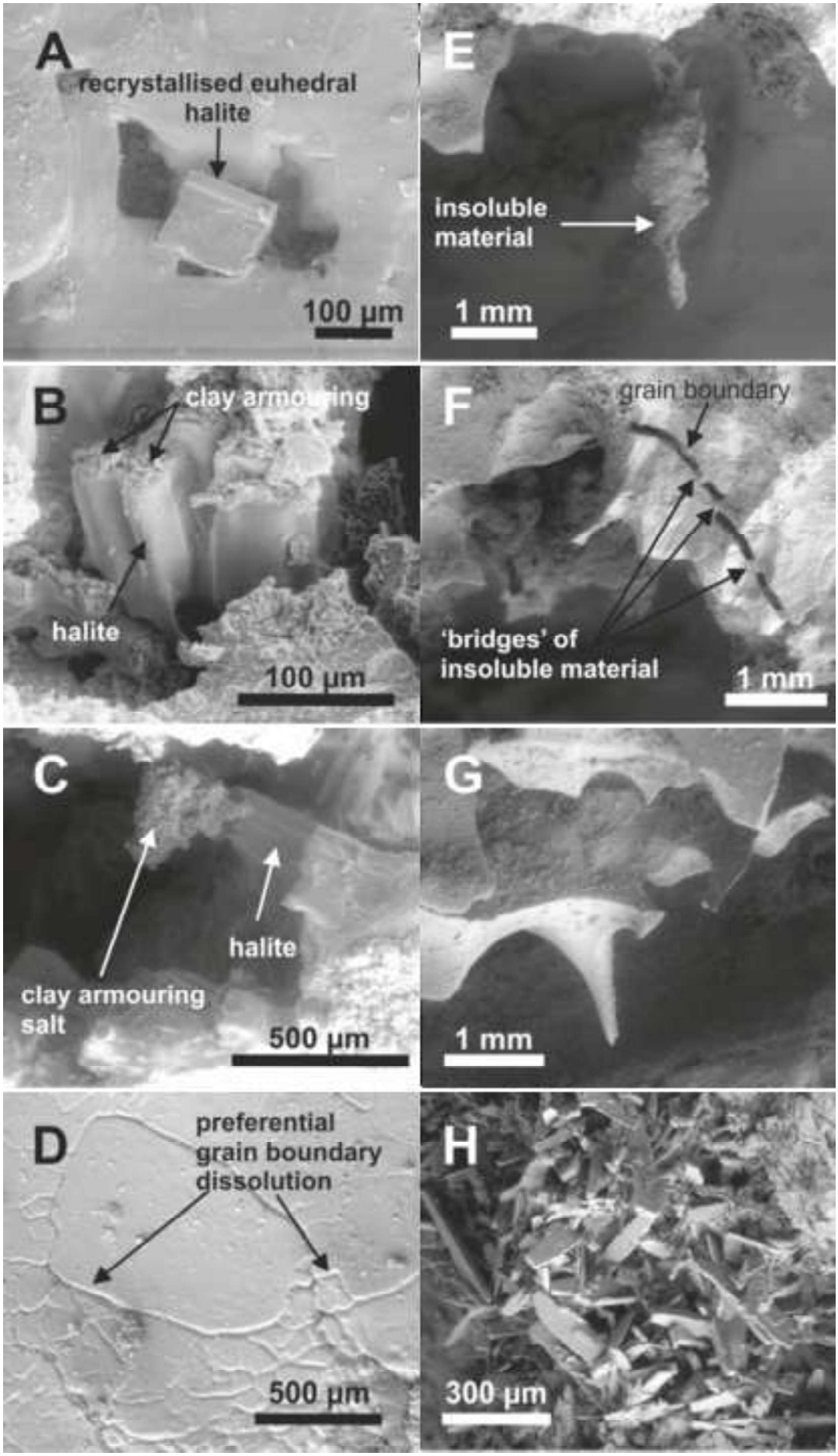

Figure 10

Click here to download Figure Fig 10.png